ChemPubSoc Europe
DOI: 10.1002/cssc.201900617
CHEMSUSCHEM Full Papers

Electrolyte Effects on the Stability of Ni–Mo Cathodes for the Hydrogen Evolution Reaction

Jochem H. J. Wijten,[a] Romy L. Riemersma,[a] Joseph Gauthier,[b] Laurens D. B. Mandemaker,[a] M. W. G. M. (Tiny) Verhoeven,[c] Jan P. Hofmann,[c] Karen Chan,[d] and Bert M. Weckhuysen*[a]

Water electrolysis to form hydrogen as a solar fuel requires highly effective catalysts. In this work, theoretical and experimental studies are performed on the activity and stability of Ni–Mo cathodes for this reaction. Density functional theory studies show various Ni–Mo facets to be active for the hydrogen evolution reaction, Ni segregation to be thermodynamically favorable, and Mo vacancy formation to be favorable even without an applied potential. Electrolyte effects on the long-term stability of Ni–Mo cathodes are determined. Ni–Mo is compared before and after up to 100 h of continuous operation. It is shown that Ni–Mo is unstable in alkaline media, owing to Mo leaching in the form of MoO_4^{2-}, ultimately leading to a decrease in absolute overpotential. It is found that the electrolyte, the alkali cations, and the pH all influence Mo leaching. Changing the cation in the electrolyte from Li to Na to K influences the surface segregation of Mo and pushes the reaction towards Mo dissolution. Decreasing the pH decreases the OH^- concentration and in this manner inhibits Mo leaching. Of the electrolytes studied, in terms of stability, the best to use is LiOH at pH 13. Thus, a mechanism for Mo leaching is presented alongside ways to influence the stability and make the Ni–Mo material more viable for renewable energy storage in chemical bonds.

Introduction

In the gradual transition from fossil fuel resources (i.e., coal, gas, and crude oil) towards more sustainable resources, such as solar and wind energy, the storage of the produced electrical energy is still a challenge.[1–3] This storage is necessary because of the intermittent nature of green energy sources, most easily explained by the day–night and summer–winter cycles of the sun. Current battery technology is not (yet) applicable at the global energy scale. Furthermore, the low energy density of batteries is not suitable for heavy transport applications, such as intercontinental airplanes, heavy-duty trucks, and large container ships. Other aspects of fossil fuel processing, such as polymer production, should be taken into account as well.[3] Thus, storage of energy in chemical bonds is a viable option that is being considered. One of the most energy-rich bonds is the hydrogen–hydrogen bond, which can be obtained by the electrolysis of water.[4] Not only is H_2 considered as a fuel by itself, it is also an important building block in the chemical industry in, for example, the Haber–Bosch process.[1,2] It is also used as a reductant in reactions, such as CO_2 conversion into CH_4 or CH_3OH.[3]

H_2 obtained by water splitting, driven by solar energy, is often dubbed a solar fuel.[4,5] To facilitate this reaction, electrocatalysts are employed, of which the most efficient currently known is Pt, owing to its high activity and stability.[1,2] However, owing to its low abundance and cost, Pt is impractical for large-scale applications and other materials are being considered.[2] Amongst these materials, one of the most promising ones is alloyed Ni–Mo, which is surmised to have a hydrogen bonding energy (HBE) similar to that of Pt, owing to the synergy between Ni and Mo in alkaline water splitting.[6] Alkaline water splitting is considered because of its relevance in industry and the availability of better-performing anodes in alkaline relative to acidic media.[2,7–14]

Several strategies are employed to increase the activity of Ni–Mo, such as nanostructuring or using nanoparticles.[15–17] It can also be combined with light-absorbing materials as a co-catalyst.[18] A lot of work is focused on studying the synthesis

[a] J. H. J. Wijten, R. L. Riemersma, L. D. B. Mandemaker, Prof. Dr. B. M. Weckhuysen
Inorganic Chemistry and Catalysis, Debye Institute for Nanomaterials Science, Utrecht University
Universiteitsweg 99, 3584 CG Utrecht (The Netherlands)
E-mail: b.m.weckhuysen@uu.nl

[b] J. Gauthier
Suncat Center for Interface Science and Catalysis
Stanford School of Engineering & SLAC
443 Via Ortega, Stanford CA 94305 (USA)

[c] M. W. G. M. Verhoeven, Dr. J. P. Hofmann
Laboratory for Inorganic Materials and Catalysis, Department of Chemical Engineering and Chemistry, Eindhoven University of Technology
P.O. Box 513, 5600 MB Eindhoven (The Netherlands)

[d] Dr. K. Chan
CatTheory Center, Department of Physics
Technical University of Denmark, Kongens Lungby 2800 (Denmark)

Supporting Information and the ORCID identification number(s) for the author(s) of this article can be found under: https://doi.org/10.1002/cssc.201900617.

of Ni–Mo by changing the morphology and composition.[11–13,19] A Ni content of 60–80% in these alloys has been found to be optimal for the activity and stability.[2,13,16,20] However, although some previous works have shown that Ni–Mo is unstable in alkaline media, the origins of this instability have not been extensively studied to date, aside from one key work by Schalenbach et al.,[20] who reported that Ni–Mo can form multiple crystal phases depending on the ratio between Ni and Mo. Furthermore, they reported that Mo can leach from the material during electrocatalysis.[8,20,21]

Herein, we present a combined theoretical–experimental study of the activity and stability of Ni–Mo as a hydrogen evolution reaction (HER) electrocatalyst. By using density functional theory (DFT) and a simple thermodynamic model of HER activity, we predict the model Ni–Mo system to be highly active towards the HER on several facets.[22] As Mo leaches, the nature of the electrolyte is expected to play a key role. To this end, we studied different commonly used electrolytes—NaOH, KOH, and LiOH—and show that the choice can play a significant role in HER performance.[2] Our calculated energies suggest Ni segregation and Mo vacancy formation to be favorable.[23–25] Experimentally, by using X-ray spectroscopy (SEM-EDX), atomic force microscopy (AFM), X-ray photoelectron spectroscopy (XPS), inductively coupled plasma atomic emission spectroscopy (ICP-AES), and UV/Vis spectroscopy, we characterized the stability of Ni–Mo materials in a variety of electrolytes and at various pH values. We confirm that Mo leaches, as reported by Schalenbach et al.,[20] and found that Mo leaches as MoO_4^{2-}. Roughening and changes in electrocatalytic activity were a result of Mo leaching. The cation in the electrolyte (K^+, Na^+, or Li^+) and the solution pH significantly influence these effects. With this work, we present an understanding of the Mo leaching phenomenon through both experiment and theory.

Results and Discussion

Theoretical activity

Density functional theory (DFT) was used to investigate hydrogen and cation adsorption, Ni and Mo surface segregation, and vacancy formation energies. Differential Gibbs free energies of hydrogen adsorption, ΔG_H, were calculated as it has been shown previously to be a good descriptor for the HER activity on a variety of materials.[22,25–28] Further details regarding the calculation of ΔG_H can be found in the Experimental Section. We use the limiting potential, determined theoretically as the potential at which all steps in the HER mechanism become exergonic, as an estimate of activity. For the HER, this limiting potential is simply defined as $U_L = -|\Delta G_H|/e$ and so the theoretical prediction of activity is maximized for $U_L = 0$ and hence $\Delta G_H = 0$ eV. This theoretically determined limiting potential has been shown to correlate well with experimental activity for several processes.[22,25–29] We chose Ni_3Mo as the model Ni–Mo system, owing to the similarity in stoichiometry to the experimental system. Figure 1 shows ΔG_H as a function of the surface hydrogen coverage, θ_H, for the three terrace facets of Ni_3Mo.

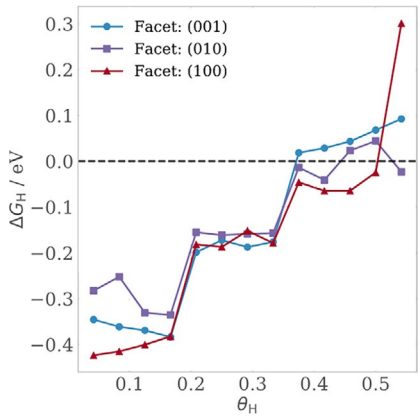

Figure 1. ΔG_H as a function of surface hydrogen coverage, θ_H.

At moderate surface coverages ΔG_H approaches zero, indicating high predicted activity towards the HER for all studied surface facets.

Experimental activity

To study Ni–Mo alloy surfaces in detail, the material was synthesized by electrodeposition on Ti substrates (see the Experimental Section).[30–32] The materials generally form amorphous, granular structures with cracks on the surface on a μm scale, which are typical structures found for electrodeposited materials (see the Supporting Information, S.1).[33] Elementally, these materials mostly consist of Ni and Mo in a 3:1 ratio, but also Na (<6%) is found in the material (see the Supporting Information, S.2); Na is present during electrodeposition, originating from the precursors used.

These samples were subjected to electrocatalysis by chronopotentiometry at $-10\ mA\,cm^{-2}$ in 1 M hydroxide solutions; note that all calculations are done on the basis of the substrate surface area. The behavior is similar for the materials employed in 1 M KOH (Figure 2a) or 1 M NaOH (Figure 2c). One difference, however, is that the catalyst in 1 M KOH takes a longer time to activate towards the optimum overpotential at about 30 h, compared with 15 h in 1 M NaOH. The absolute overpotential changes from 0.18 to 0.13 V, it then stays stable for several days before increasing again. The low overpotential shows it is indeed active as suggested by theory and previous studies.[2,7–14]

Stability: Theoretical considerations

To investigate the origin of the changing overpotential, we investigated the stability of the Ni–Mo system under HER conditions. Cation and hydroxyl adsorption free energies, ΔG_{ads} and ΔG_{OH}, respectively, were calculated under operating conditions ($U = -0.15$ V vs. reversible hydrogen electrode, RHE, pH 13) to determine if they play a role in the changes of surface morphology.

The calculations were done with Ni_3Mo as the system of choice. X-ray diffraction was attempted (see the Supporting In-

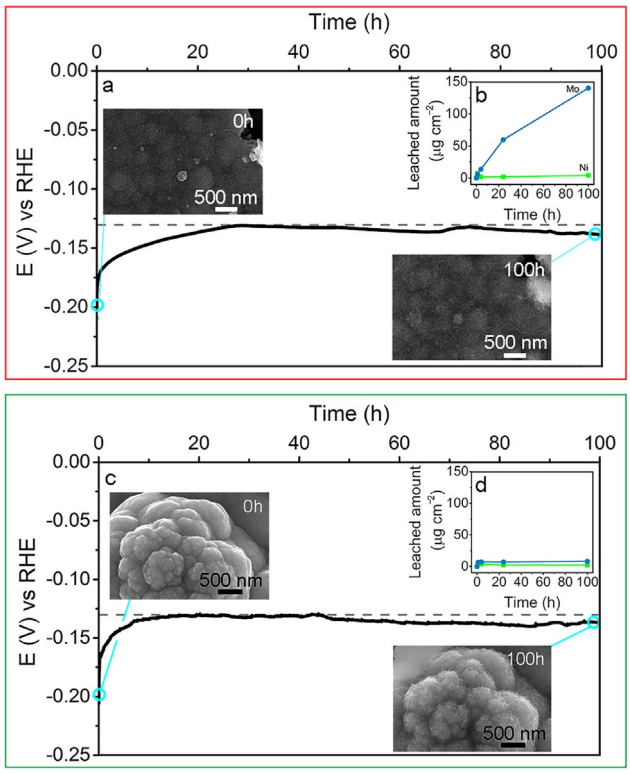

Figure 2. Boxed in red are the experiments performed in 1 M KOH: a) Chronopotentiometric curve obtained at $-10\ mA\,cm^{-2}$ for Ni–Mo electrodeposits. The SEM images show the Ni–Mo surfaces after different times of catalysis, with 0 h and 100 h taken on the same sample (see the Supporting Information, S.1, for images of other unspent samples). b) Amount of Ni and Mo found in spent electrolytes as determined by ICP-AES per cm^2 of electrode. Boxed in green are the experiments performed in 1 M NaOH: c) Chronopotentiometric curve obtained at $-10\ mA\,cm^{-2}$ for Ni–Mo electrodeposits. The SEM images show the Ni–Mo surfaces after different times of catalysis, with 0 h and 100 h taken on the same sample (see the Supporting Information, S.1, for images of other unspent samples). d) Amount of Ni and Mo found in spent electrolytes as determined by ICP-AES per cm^2 of electrode.

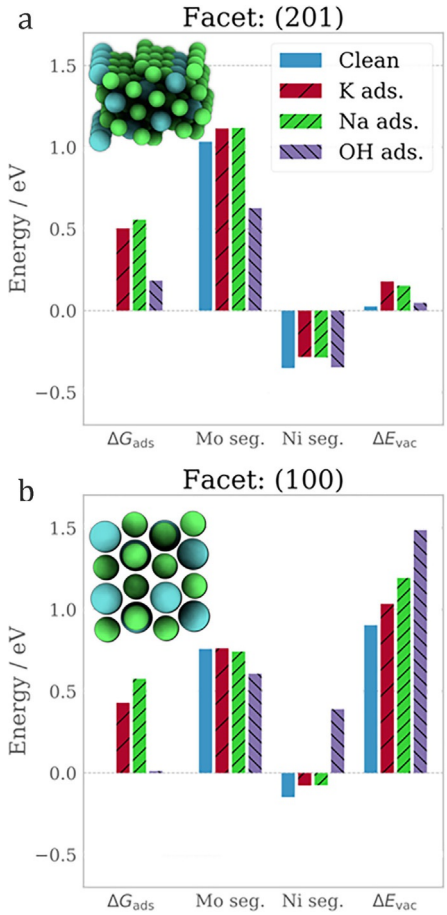

Figure 3. DFT investigation into the thermodynamics of surface restructuring, calculated under operating conditions ($U = -0.15$ V vs. RHE, pH 13). a) Energetics at a stepped Ni_3Mo surface. b) Energetics for a Ni_3Mo terrace surface.

formation, S.3) but the crystallites were found to be too small, or amorphous, to be conclusive on the exact X-ray structure. With EDX, a stoichiometric Ni/Mo ratio of 3:1 was found, and this was used for the calculations with the assumption that this refers to the crystal structure.

Figure 3 shows these energies for a step and terrace termination of Ni_3Mo. Similar plots for terrace facets (0 1 0) and (0 0 1) can be found in the Supporting Information (S.4). We find that cations bind unfavorably to both steps and terraces at these potentials. Assuming a Boltzmann distribution, the expected coverage of cations θ_{ion} is therefore effectively 0. However, solvent stabilization may allow cations to adsorb at small coverages at more negative potentials. Similarly, *OH binds unfavorably on the step, and weakly on the terrace. Solvent stabilization again may allow some small coverage of *OH.

The energy to segregate Mo to the surface was then calculated according to Equation (1):

$$\Delta E_{seg,Mo} = E_{seg} - E_{clean} - (E_{Mo} - E_{Ni}) \quad (1)$$

where E_{seg} is the energy of a surface where one surface Ni atom is replaced with one bulk Mo atom, E_{clean} is the clean surface, E_{Mo} is the energy of one Mo atom in Ni_3Mo relative to bulk Ni, and E_{Ni} is the energy of one Ni atom in Ni_3Mo relative to bulk Mo.

Similarly, segregation energies for bringing Ni to the surface from bulk Ni_3Mo, while sending a surface Mo atom to a solvated molybdate ion, were determined according to Equation (2):

$$\Delta E_{seg,Ni} = E_{seg} - E_{clean} - [E_{Ni} - (E_{Mo(s)} + \Delta E_{Mo,diss})] \quad (2)$$

where $E_{Mo(s)}$ is the energy of a molybdenum atom in its pure solid phase and $\Delta E_{Mo,diss}$ is the energy of the dissolution reaction, which converts Mo(s) into a molybdate ion, details of which can be found in the Supporting Information. Molybdate is considered as it is the most likely to form at pH 14, under the studied potentials, according to the Pourbaix diagram.[34]

The energy required to form a Mo vacancy on the surface by dissolution of Mo, ΔE_{vac}, was calculated according to Equation (3):

$$\Delta E_{vac} = E_{vacancy} - E_{clean} - (E_{Mo(s)} + \Delta E_{Mo,diss}) \quad (3)$$

Here, $E_{vacancy}$ is the energy of the surface with a vacancy, and E_{clean} is the clean surface. The segregation and vacancy formation energies were calculated both on clean slabs and in the presence of cations and OH*. These are tabulated in Figure 3.

We find that it is energetically unfavorable to enrich the surface in Mo while enriching the bulk in Ni, regardless of cation adsorption. Additional results for cation adsorption can be found in the Supporting Information (S.4). We do find, however, that *OH can significantly stabilize Mo surface enrichment, although it is still unfavorable energetically. This is likely due to molybdenum's high oxophilicity. Ni enrichment, however, is generally energetically favorable, consistent with experimental observation, as discussed in the following. We find that the formation of a Mo vacancy on the surface through dissolution to molybdate is feasible on the step, but not on the terrace. Because the films in this study are highly amorphous and are likely to contain sites less coordinated than the step presented here, we expect the Mo conversion to molybdate to occur without an applied potential.

Stability: Experimental characterization

Leaching of Mo was further confirmed experimentally. On a larger scale, SEM was performed on the samples at several time intervals. In both the case of NaOH and of KOH, after a long time (100 h) of operation, edges and other nanoscaled features form on the material, which can be linked to the vacancy formation described in Figure 3. This effect is similar to that observed during anisotropic etching of noble metals, and thus could be linked to Mo leaching.[35,36]

The similarity with anisotropic etching led us to measure ICP-AES (see the Supporting Information, S.5) of the electrolytes after catalysis, to observe the possible Mo or Ni leaching (see Figure 2b,d for 1 M KOH and 1 M NaOH, respectively). Indeed, Mo leaches, most obviously when using KOH as an electrolyte. Leaching in KOH starts slower than in NaOH during the first hour, but continues to a higher value of 1.84 μmol Mo after 100 h. In the case of NaOH, it leaches to a value of 0.09 μmol Mo after just 1 h, but after that no more leaching takes place. In either situation, both activity and stability are superior to pure Ni and Mo electrodes (see the Supporting Information, S.6).

Despite the significant difference in Mo leaching between KOH and NaOH electrolytes, we observe that the chronopotentiometry does not change much after about 30 h of operation, suggesting a steady state is achieved. Furthermore, as shown in Figure 3, according to DFT, neither Na^+ or K^+ adsorbs, suggesting that this is not a pathway through which leaching is influenced. The apparent roughening observed in SEM is a suitable explanation for the slight decrease in overpotential observed during the beginning of the chronopotentiometry: the available surface area increases and thus activity increases. To quantify the roughening process, double layer capacitance measurements and AFM were employed. First, this capacitance is not only a function of surface area: the specific capacitance of a material depends on the composition as well.[37–39] Previous research shows that the Ni^{2+}/Ni^{3+} redox couple can also be used to determine surface areas,[20] but we find, that as the surface concentration of Ni changes, that this approach likewise is limited. Furthermore, to be able to study in detail what happens during HER catalysis, applying oxidizing potentials might result in electrochemical processes that are usually not found for the Ni–Mo system under HER conditions such as anodic etching.

As neither approach of determining the surface area is ideal, we attempt to, at least, exclude the possibility that differences in capacitance values are due to small differences between samples, by performing experiments where every 30 min of catalysis alternates with double layer capacitance measurements (Figure 4). Immediately, it is clear that there is an influence from the electrolyte. In KOH it takes longer for the catalyst to reach the optimum in overpotential (take note of the different *x*-axes). During this process, the capacitance increases with a rate of 2.3 mF h^{-1} before levelling off at a normalized capacitance of 13 mF, whereas in NaOH this rate is only 1.3 mF h^{-1} and it levels off at only 4 mF. Although these data cannot be directly related to roughness, it shows the change of the material is gradual during HER catalysis and that it occurs on the same timescale as the change in overpotential. With AFM, we found that the increase in surface area after 24 h is 23% when using NaOH (Figure 4d). This is significantly less than the factor four increase found with the capacitance measurements, immediately proving that the capacitance cannot be directly linked to surface roughness. In the case of KOH (Figure 4b), it is even more extreme and a decrease in surface area is observed.

It should be noted that the root-mean-square (RMS) determination (see the Supporting Information, S.7) is difficult owing to the presence of micrometer-scale cracks. Furthermore, features on the nanometer scale, such as possible pores having formed are not taken into consideration on this scale. We selected spots based on their relative lack of large features at the beginning. Nevertheless, as seen in the AFM images of Figure 4b, large changes can occur owing to cracking or removal of whole grains as a result of flaking, which will influence the determined RMS significantly. Furthermore, experiments on pure Ti, pure Ni, and pure Mo show that the specific capacitance of Mo is higher than that of Ni (see the Supporting Information, S.6) meaning this can be related to more Mo being present at the surface. It furthermore shows that Ti has no change in capacitance, excluding this as a possible explanation for the observations.

The large change in surface capacitance and the observed leaching led us to study the surface in more detail. As mentioned before, with EDX Na is present at the surface, and furthermore, after catalysis, this amount is either increased (NaOH) or replaced by K (KOH) (see the Supporting Information, S.2). To find what is really occurring on the surface itself and in the first few 100 nm, we used XPS depth profiling (see Figure 5a). Prior to catalysis, the samples contain Na, Ni, and Mo homogeneously dispersed throughout the first 600 nm, with only the surface being significantly higher in Na and Mo content. Furthermore, the Mo content is higher near the surface (40%) than what was found with EDX (25%), which is ef-

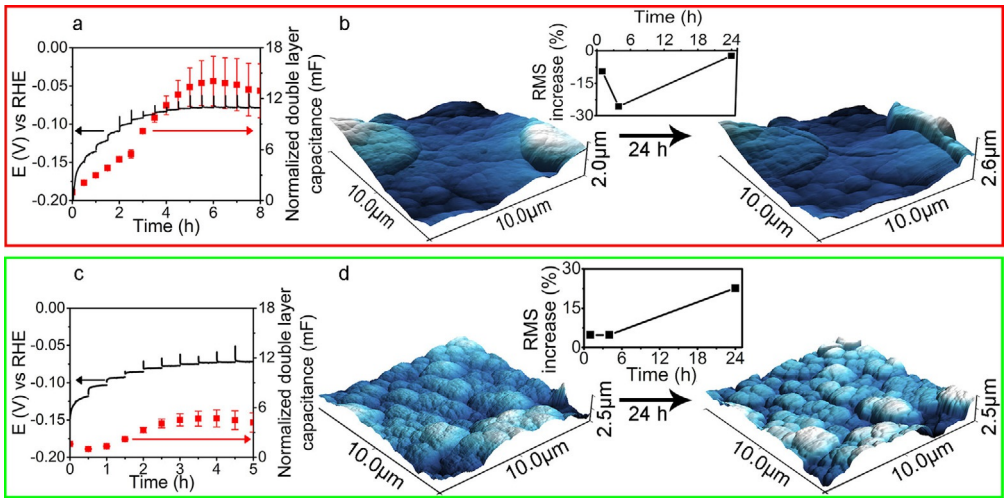

Figure 4. a) Stepped chronopotentiometry in KOH (black, left axis) alternated with double layer capacitance measurements (red squares, right axis). b) AFM images obtained prior (left) and post (right) catalysis in KOH for 24 h. Above the image, the increase in RMS is shown, where negative values correspond to a decrease. c) Stepped chronopotentiometry in NaOH (black, left axis) alternated with double layer capacitance measurements (red squares, right axis). d) AFM images obtained prior (left) and post (right) catalysis in NaOH for 24 h. Above the arrow, the increase in RMS is shown, where negative values correspond to a decrease.

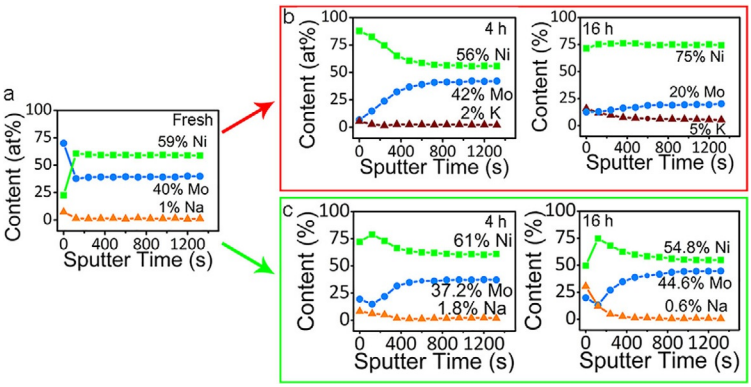

Figure 5. a) XPS depth profile of a fresh Ni–Mo surface. In all cases, a sputter rate of 0.50 nm s^{-1} was assumed (based of Ta_2O_5). b) XPS depth profile of Ni–Mo spent in 1 M KOH after 4 h and 16 h. c) XPS depth profile of Ni–Mo spent in 1 M NaOH after 4 h and 16 h. In all Ni (green squares), Mo (blue circles), and Na (orange triangles) or K (purple triangles) are shown. Other elements (O, C) have not been taken into account in the calculation of the ratios. Related spectra taken at 0 nm depth can be found in the Supporting Information, S.9.

fectively a bulk technique for these samples. The observation of Mo being more concentrated on the surface points towards surface segregation, as has been reported before.[23,24]

After chronoamperometry in 1 M KOH (Figure 5 b), already after 4 h, the Mo content has decreased significantly in the first 400 nm (from 40% to 15% at 60 nm depth). This is more significant even after 16 h, reaching beyond the probing depth of 660 nm. At the same time, Na was completely gone after 4 h and instead K is found, most prominently on the surface. In NaOH (Figure 5 c), the same effect occurs but the extent of the leaching of Mo is less. Mo contents decrease over time as well in NaOH, mostly from the top layers, but in contrast with KOH electrolytes; even after 16 h, leaching barely occurred after 500 nm.

In NaOH and in KOH, the alkali cation infiltrated the surface in higher concentrations than was the case prior to catalysis. Its presence, however, is much more contained to the surface for Na than for K, being higher at the top layers but almost absent after 200 nm, whereas for K it is more homogeneously present after 16 h up to at least 660 nm. This implies there is a different rate of the formation of porosity into which the electrolyte infiltrates. This agrees with the formation of Mo vacancies according to DFT and the different Mo leaching rates found. The higher values for Na in the top layer than for K can be related to the difference in ion size (Na^+ is smaller than K^+ and thus more would fit in a pore of the same size). Furthermore, the samples tested in NaOH retain the property that the Mo content directly at the surface is slightly higher than in the layer beneath it. Thus, the presence of Na or K influences Mo surface segregation. These observations agree with the capacitance measurements, where Ni and Mo atoms influence the specific capacitance more than Na and K, as the surface ratio of Ni/Mo changes much more in KOH than in NaOH. Owing to the role of the cations, we also made catalysts from K-based electrodeposition baths, but owing to their poor performance, we decided not to study them in detail (see the Supporting Information, S.8).

Prior to catalysis, the surface consists mostly of Ni^{II} hydroxide, whereas most of the Mo is Mo^{VI} with a small amount of Mo^{IV} and a few percent of metallic Mo. After catalysis in either electrolyte, the Ni retains its phase, whereas Mo is (almost) fully oxidized to Mo^{VI} after exposure to air (see the Supporting Information, S.9). Information on the deeper layers regarding oxidation states is disregarded, as the sputtering to measure deeper layers is a reducing process, possibly reducing the Mo to the metallic state as well.

Leaching mechanism

To explore in more depth the mechanism of Mo leaching, we performed UV/Vis spectroscopy on spent electrolytes (Figure 6). In both KOH and NaOH, UV/Vis bands are visible, characteristic for the presence of MoO_4^{2-} species, effectively proving that the leaching indeed occurs by the formation of MoO_4^{2-}. Leaching even occurs without applied potential (see the Supporting Information, S.5), thus we suggest $Mo + 2OH^- + 2H_2O \rightarrow MoO_4^{2-} + 3H_2$ to be the leaching mechanism. As Mo leaches as MoO_4^{2-}, the difference between K and Na could be explained by the solubility constants of K_2MoO_4 and Na_2MoO_4 on top of the observed influence of surface segregation. To ensure the solubility constants we use are relevant, these were determined in the electrolytes used. The solubility of K_2MoO_4 (0.76 g L^{-1}) is significantly higher than that of Na_2MoO_4 (0.39 g L^{-1}) independent of the pH used (pH 8, 11, and 14), except for 6 M solutions. In the case of 6 M solutions, the solubility was found to be lower (0.43 g mL^{-1} and 0.13 g mL^{-1} for K_2MoO_4 and Na_2MoO_4, respectively), which is likely due to the higher concentration of K^+ or Na^+ ions in the electrolyte. This can explain the difference in behavior despite the lack of differences in the calculations.

To confirm that the suggested reaction takes place, and that it is a nonfaradaic process as is thermodynamically suggested, the faradaic efficiency (F.E.) was determined. By using gas chromatography (GC), we find that during the first few hours of HER catalysis in hydroxide solutions, the F.E. is higher than 100% in the case of 1 M KOH. This is shown in Figure 7a. This agrees with the proposed reaction mechanism where hydrogen forms without consuming electrons from the circuit, thus forming more hydrogen than the applied current would suggest. For 1 M KOH, it tops out at 122%, after which it drops slowly to a value corresponding to 103% F.E. In 1 M NaOH, however, no such peak in F.E. is observed and it is constant at a F.E. of 101%, corresponding to the lower extent of Mo leaching.

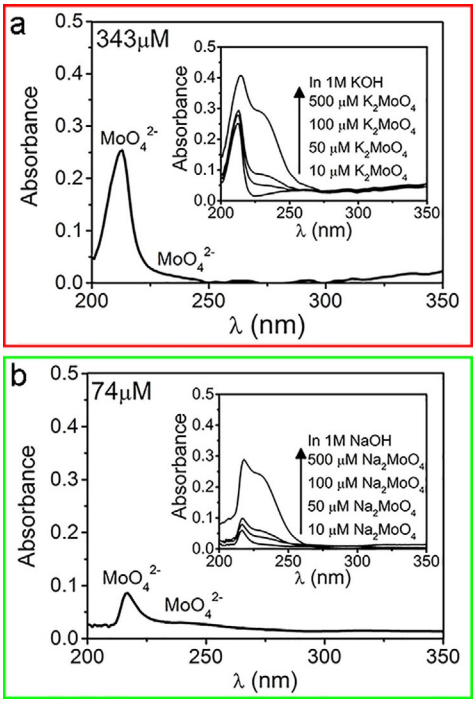

Figure 6. a) UV/Vis spectrum after 100 h of catalysis in 1 M KOH. The inset shows spectra of K_2MoO_4 in 1 M KOH as references. b) UV/Vis spectrum after 100 h of catalysis in 1 M NaOH. The inset shows spectra of K_2MoO_4 in 1 M NaOH as references.

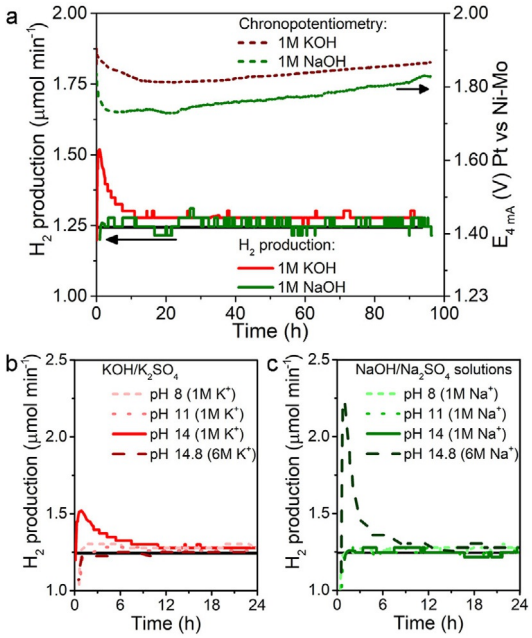

Figure 7. a) Hydrogen production found for Ni–Mo in 1 M KOH (red) or 1 M NaOH (green) at 4 mA; the black line shows the theoretical amount expected. The dashed lines show the chronopotentiometric curves of these experiments. b) Hydrogen production in KOH at different pH values. c) Hydrogen production in NaOH at different pH values.

Effect of pH

In the case of KOH, it is possible to suppress the additional formation of hydrogen by lowering the pH, making the Mo leaching reaction less likely to occur. This is shown in Figure 7b. Meanwhile, increasing the pH for 1 M NaOH, owing to the higher concentration of hydroxide ions, results in the peak in F.E. coming up as well for that electrolyte (Figure 7c). Interestingly, in 6 M KOH, the peak in hydrogen production is absent. The explanation we propose is that in the case of 6 M KOH, the material leaches directly from the Ni–MoO_3 phase resulting in the reaction being $MoO_3 + 2OH^- \rightarrow MoO_4^{2-} + H_2O$. In the other solutions, leaching takes place from the metallic phase, which is present owing to the reducing potential being applied during these experiments.[34] In contrast, the Mo leaching observed with ICP-AES (Figure 8) is significantly lower in 6 M NaOH and 6 M KOH, although it should be noted that the higher concentration of easily ionizable alkali ions (6 M versus 1 M) can significantly suppress the signal of other analytes.[40] From ICP-AES, we also observe that at pH 8 the leaching of Ni becomes significant as well, as can be seen in Figure 8. Inter-

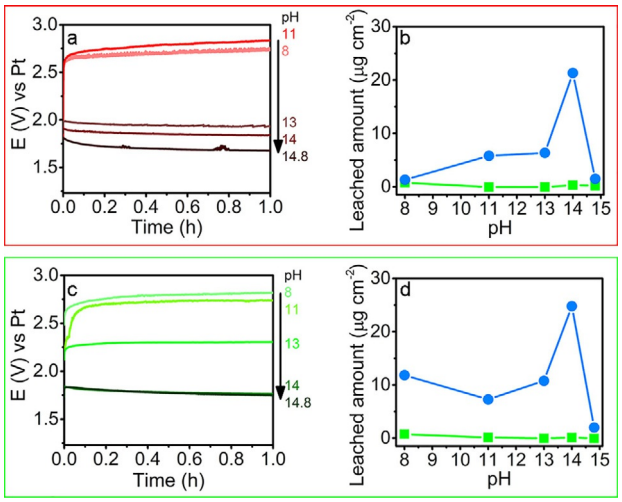

Figure 8. a) The first hour of the chronopotentiometric curves in 1 M K^+ (KOH/K_2SO_4) solutions of varying pH. b) The observed Mo (blue circles) and Ni (green squares) leaching after 24 h of operation at $-10\ mA\,cm^{-2}$ in K^+ solutions of varying pH. c) The first hour of the chronopotentiometric curves in 1 M Na^+ ($NaOH/Na_2SO_4$) solutions of varying pH. d) The observed Mo (blue circles) and Ni (green squares) leaching after 24 h of operation at $-10\ mA\,cm^{-2}$ in Na^+ solutions of varying pH.

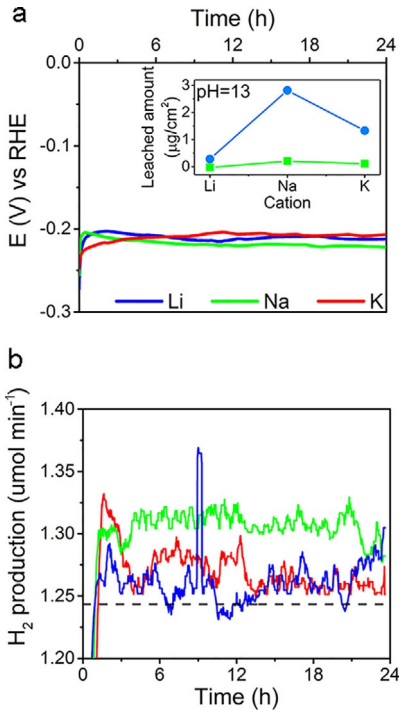

Figure 9. a) Chronopotentiometric curves in different 1 M M^+ solutions at pH 13 (MOH/M_2SO_4) with Li (blue), Na (green), K (red), showing nearly no variation. The inset shows Mo (blue circles) and Ni (green squares) leaching. b) H_2 production as observed by in-line GC. The dotted line shows the expected value based on the applied current.

estingly, although the Mo leaching decreases with decreasing pH, we also observed that this effect was far less significant for NaOH compared with KOH, meaning that the stability is less at lower pH values for NaOH than for KOH (see Figure 8).

Furthermore, for NaOH, at a pH of 8, the Mo leaching increases again. This might relate to the increased Ni leaching, which makes more Mo surface available.[34] This is related to the earlier observations of leaching in Na being faster, but less deeply penetrating. More Mo becomes available owing to Ni leaching and in NaOH this increase in available Mo leaches faster than in KOH. In the case of the experiments performed at lower pH values, the electrolytes acidify owing to the Mo being leached to a concentration of about 20 μM. This also results in 40 μM of OH^- being consumed, resulting in pH 4–5. This also explains why Ni leaching started in electrolytes starting from pH 8. However, the potential role of SO_4^{2-} ions in this acidification cannot be excluded; these ions result from M_2SO_4, which was added to maintain a constant alkali cation concentration.

Mo leaches even less in LiOH than in KOH and NaOH (Figure 9). Although, as mentioned before, the leaching is more prominent in NaOH than in KOH on a timescale of 24 h at lower pH values, in LiOH this is appreciably less. The F.E. as observed with GC confirms this: 101.5% of the theoretical value over the course of 24 h in Li, whereas for K and Na this is 102.1% and 105.0%, respectively. Furthermore, the shape of leaching differs between the materials: a sharp peak is observed for KOH, similar to other pH values, whereas a broad, low peak forms for NaOH and no observable peaking results in the case of LiOH. Nevertheless, the chronopotentiometric curves look similar in all cases and the morphological changes are observed in all cases as well (see the Supporting Information, S.10).

In Figure 10, the XPS depth profiles confirm the earlier statement that lighter alkaline elements infiltrate more easily into the alloy, as Li contents reach 85% directly on the surface whereas this is 47% and 20%, respectively, for Na and K. From these data, the difference in leaching behavior at pH 13 compared with pH 14 can be explained as well: the highest leaching experiment was performed in NaOH and in contrast with KOH and LiOH in this case the Mo/Ni ratio increases instead of decreases. This is believed to be a result of Mo surface segregation, which has been described previously.[23,24] In the cases of KOH and LiOH, the Mo/Ni decreases towards the surface, as was also the case for the experiments at pH 14. This means that Mo transport to the surface is less in these cases, as seen by the elemental ratios stabilizing earlier into the material. This

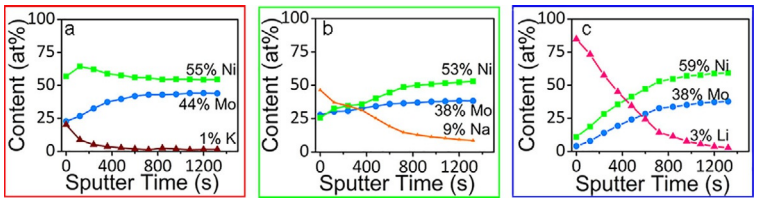

Figure 10. Elemental ratios up to 660 nm into the material from the surface as determined by XPS after 24 h of catalysis in 1 M M^+ solutions at pH 13 for a) M = K, b) M = Na, and c) M = Li. A sputter rate of 0.50 $nm\,s^{-1}$ (based on Ta_2O_5) was assumed for determining the *x*-axis.

lessened segregation left less Mo exposed to leach into the electrolyte.

Conclusions

Ni–Mo cathodes perform exceptionally well in hydrogen evolution reaction (HER) electrocatalysis and exhibit high performance stability, as the overpotential of operation only changes slightly during 100 h of catalysis. Density functional theory (DFT) calculations show Ni–Mo low-index facets to have nearly thermoneutral H adsorption free energy, which is consistent with the observed high Ni–Mo activity. Furthermore, the theoretical calculations also suggest both Ni segregation and Mo vacancy formation to be favorable even without the influence of an applied potential. This observation was confirmed by catalyst characterization results. The activation observed at the start of HER operation is non-faradaic and due to Mo leaching through the reaction $Mo + 2OH^- + 2H_2O \rightarrow MoO_4^{2-} + 3H_2$. This results in an overall increase in surface area and thus an apparent decrease in absolute overpotential. Although the material operates stably for at least a week, future research on longer timescales should show if the leaching would be detrimental for real long-term performance stability. Furthermore, the leaching results in undesired contaminants in operating systems and we have shown how simple changes to the electrolyte (by changing the monovalent cation) can already significantly suppress the Mo leaching without hugely influencing the overall HER performance (Figure 11).

The influence, we found, can be directly related to the observed mechanism of leaching. Changing the electrolyte cation from Li to Na to K influences the surface segregation of Mo, and thereby pushes the reaction towards Mo dissolution by increasing the surface concentration of Mo. Decreasing the pH decreases the concentration of OH^- and in this manner inhibits the leaching reaction. This is, however, only valid down to a certain value as the leaching reaction consumes OH^- and acidifies the solution, which becomes significant at pH values closer to neutral. The acidification destabilizes Ni instead, similarly destroying the HER material. Of the electrolytes studied, in terms of stability, the best to use is LiOH at pH 13.

Experimental Section

Computational details

All calculations were performed by using the Vienna ab-initio simulation package (VASP).[41–43] Core electrons were described by PAW pseudopotentials,[44,45] whereas valence electrons were expanded as plane waves with a kinetic energy cut-off of 500 eV. Exchange-correlation interactions were described by using the RPBE functional.[46] For surface calculations, the Brillouin zone was sampled by using a 4×4×1 Γ-centered Monkhorst–Pack[47] k-point mesh (6×6×6 was used for bulk Ni_3Mo, and 12×12×12 was used for bulk Ni, Mo, K, and Na). Ni_3Mo was chosen as a model system, owing to the 3:1 ratio found by EDX (see the Supporting Information, S.2). Crystalline unit cells were used, considering it is likely microcrystalline domains are present.[48,49] Further details of the simulations, including a description of the computational hydrogen electrode[50] and analogous reference electrodes for cations can be found in the Supporting information. Predominant surface terminations and facets of Ni_3Mo were determined by using the Bravais–Friedel–Donnay–Harker (BFDH) algorithm.[51] The facets (0 0 1), (0 1 0), and (1 0 0) were found to be equally likely, and so all three facets were considered in our theoretical studies. To consider the polycrystalline nature of the films, a stepped surface was also considered for vacancy formation, cation adsorption, and segregation energies.

Materials

All materials were used as received without further purification. $NiSO_4 \cdot 6H_2O$ (ReagentPlus, >99% pure), $NaMoO_4 \cdot 2H_2O$ (ACS reagent, >99% pure), NaOH (99.99% trace metals, semiconductor grade), KOH (ACS reagent, >85% pure), $LiOH \cdot H_2O$ (99.95% trace metals), Na_2SO_4 (ACS reagent, ≥99.0%), K_2SO_4 (ReagentPlus, ≥99.0%), $Li_2SO_4 \cdot H_2O$ (BioUltra, ≥99.0%), and $Na_3C_6H_5O_7 \cdot 2H_2O$ (sodium citrate, ACS reagent, >99% pure) were received from Sigma–Aldrich. NH_3 28–30% (ACS reagent, ph. Eur. for analysis) was obtained from Emsure. In all experiments deionized water was used.

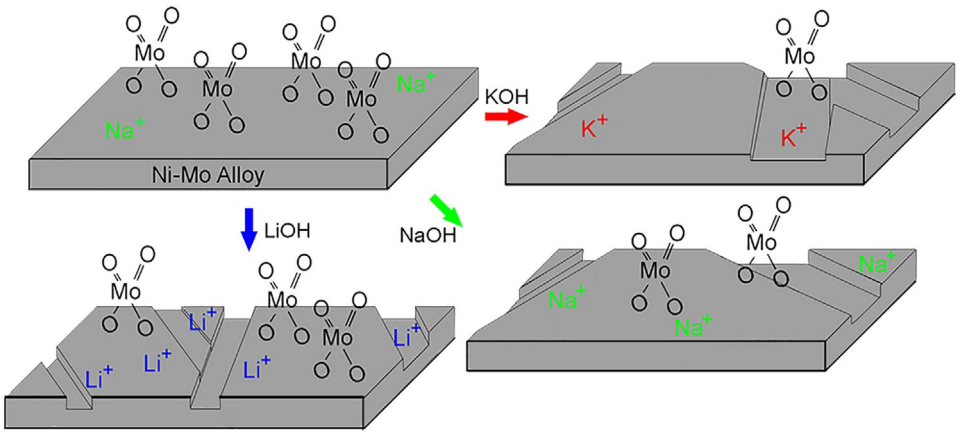

Figure 11. Schematic overview of the results, showing the Ni–Mo alloy with surface MoO_x, which, after HER catalysis, is etched by a loss of Mo and infiltrated by the monovalent cations present in the electrolyte.

Electrodeposition

Ti stubs (99.99+%, Goodfellow, machined to 1.257 cm^2 round substrates of similar shape as SEM stubs, in the Supporting Information, S.11) were fixed in a three-electrode cell for electrodeposition. Prior to electrodeposition, these were polished with SiC paper with increasing grit (500, 1200, 4000), they were then cleaned by sonication in three steps of 15 min each, first in 1:1 ethanol/acetone, then 2 M HNO_3, and finally deionized water. Electrodeposition was performed galvanostatically by using an Ivium Compactstat at a current of −100 mA for 1200 s, while stirring at 400 rpm. As a counter electrode, a Pt mesh (Mateck, 99.9%+) was used and as a reference electrode, 3 M Ag/AgCl (BASi) was used. The plating bath used contained 0.3 M $NiSO_4$, 0.2 M Na_2MoO_4, and 0.3 M $Na_3C_6H_5O_7$ in demineralized water (100 mL). To this, NH_3 (10 mL) was added to obtain a pH of 9.2. First, the metal precursors were dissolved in water through stirring, and then NH_3 was added to adjust the pH. Prior to the syntheses, the baths were purged with Ar for 15 min, and a gentle Ar flow was kept over the solution during electrodeposition.

Electrochemical characterization

Electrochemical testing on samples was done as follows. The samples were loaded in three-electrode cells (see the Supporting Information, S.11) with a Pt mesh counter electrode and a 3 M Ag/AgCl [Metrohm, shielded, −0.207 V vs. SHE, which is −1.033 V vs. RHE (pH 14), and −0.974 V vs. RHE (pH 13)] reference electrode. The possibility for Pt leaching was evaluated with XPS and EDX and it was not detected (see the Supporting Information, S.12).[52] Furthermore, the activity and observed effects are similar when Au is used as a counter electrode (see the Supporting Information, S.13). Glassy carbon was also tested, but as reported before, was unstable under these conditions, despite other works calling for this electrode to be preferable (see the Supporting Information, S.13).[52,53] Thus, it is clear that the counter electrode should always be evaluated as they behave differently in different electrolytes. 1 M MOH is used as an electrolyte at pH values of 14. Other electrolytes were made with MOH and M_2SO_4 to maintain a concentration of 1 M alkali cations (M^+). First, double layer capacitance measurements were performed between −0.7 V and −0.9 V vs. Ag/AgCl at 100, 200, 300, 400, and 500 mV s^{-1} for three cycles each. Following this, a linear sweep was performed at 50 mV s^{-1} from −1 V to −1.3 V vs. Ag/AgCl to confirm no polluting electrochemical processes take place (data not shown). Finally, chronopotentiometry was performed for varying lengths of time (1, 4, 24, or 100 h) at −12.57 mA (−10 mA cm^{-2}). The linear sweep and double layer capacitance measurements were performed again. Double layer capacitance values were obtained by taking the difference between the forward and backward current of the third scan. Data was averaged between 0.795–0.805 V for each point. The resulting double layer thickness was then plotted versus the scan rate. The linear fit of these points yield the capacitance. The stepped capacitance measurements were performed by alternating 30 min-long chronopotentiometric measurements with the five cyclic voltammetry measurements. This was done over the course of 24 h. The data after the capacitance value levels off is not shown as linear fitting beyond that point could no longer be called satisfactory as the points were approaching a second-order function. Gas chromatography (GC) analysis was done with a H-cell with a Nafion perfluorinated membrane (Nafion 117, 0.007 inch thick, Sigma–Aldrich) loaded with the electrodes and 1 M KOH (see the Supporting Information, S.11). This was purged with 2 mL min^{-1} N_2 (5.0), 0.1 mL min^{-1} Kr (5.0) on the O_2 side and 2 mL min^{-1} Ar (5.0), 0.1 mL min^{-1} Kr on the H_2 side. This was bubbled past the samples through a glass frit. The O_2 electrode was the working electrode (WE), the H_2 electrode was the counter electrode (CE)/reference electrode (RE). A current of 4 mA cm^{-2} was maintained for 96 h. GC was obtained by using Global Analyzer Solutions Compact GC 4.0 from Interscience with separate channels for H_2 and O_2. H_2 was analyzed by using a 75 μL sample loop injecting into a 5 m, 0.53 mm MXT-Q-bond then a 10 m 0.53 MXT-Msieve column and detected with a TCD. O_2 was injected by using a 50 μL loop through different columns of the same type and analyzed with a separate TCD. An injection was done each minute, with about 10 s delay between each injection. For each injection, Kr was used as an internal standard.

Structural characterization

UV/Vis spectroscopy was performed by using an Avantes DH-2000-BAL Deuterium lamp and an Avantes StarLine AvaSpec-2048 L spectrometer using a liquid-immersed probe head. The spectra were obtained in the range 200–500 nm using 1 M KOH or 1 M NaOH as a reference. Inductively coupled plasma atomic emission spectroscopy (ICP-AES) was performed by using an Optima 8300 instrument from PerkinElmer and an average of three samples was used. Electrodeposited samples were dissolved in 2% HNO_3 (10 mL) before oxidation. These were diluted with 2% HNO_3 to achieve optimal measurement ranges. Electrolytes were decreased in pH by adding 1 mL 65% HNO_3 per 10 mL electrolyte, resulting in approximately 2% HNO_3. Ni (231.604 nm), K (766.491 nm), Na (589.592 nm), Ti (334.187 nm), and Mo (202.095 nm) were then measured. Scanning electron microscopy (SEM) with energy dispersive X-ray (EDX) spectroscopy was performed with a FEI Helios nanolab 600 DualBeam with an Oxford Instruments Silicon Drift Detector X-Max energy dispersive spectroscope. EDX mapping was performed with an electron beam of 15 kV and 0.8 nA. All SEM imaging was done by using secondary electrons at 15 kV and 0.8 nA. Wide images were first shot to ensure the larger magnifications were taken at representative areas of the material (data not shown for brevity). X-ray photoelectron spectroscopy (XPS) measurements were carried out with a Thermo Scientific K-Alpha instrument, equipped with a monochromatic small-spot X-ray source and a 180° double focusing hemispherical analyzer with a 128-channel detector. Spectra were obtained by using an aluminium anode ($Al_{K\alpha}$ = 1486.6 eV) operating at 72 W and a spot size of 400 μm. Scans were measured in snapshot mode. The background pressure was 2×10^{-8} mbar and during the measurement 3×10^{-7} mbar Argon because of the charge compensation dual beam source. The sputtering parameters were as following: ion energy = 2000 eV, high current, sputter rate estimate (Ta_2O_5) = 0.50 nm s^{-1}, sputter time = 120 s $level^{-1}$, number of levels = 12. Binding energy calibration for all samples was performed by setting the C 1s (sp^3) binding energy of adventitious carbon to 285.0 eV. Fitting of the spectra (BE, FWHM, peak shape, asymmetry, number of species) was performed with CasaXPS. Content percentages of Ni, Mo, Na, and K were determined by finding the area of their respective spectra and dividing this by the sensitivity factor, which is specific to the element. This gives the relative area for each element. All relative areas of the elements of interest (excluding C and O) together are defined as 100%. Atomic force microscopy (AFM) measurements were performed with a NT-MDT NTEGRA Spectra instrument, using silicon NSC-16 tips (F = 45 N m^{-1}, f_{res} = 190 kHz) in tapping mode. Samples were marked by using a scalpel, and an optical system was used to find the same scanning spots pre- and post-catalysis. Flattening and masking were done by using Gwyd-

dion.[54] Surface roughnesses (as root-mean-square, RMS) were determined by using the program "Statistical quantities" on exclusively the masked areas (see the Supporting Information, S.7).

Acknowledgements

B.M.W. would like to thank the Netherlands Organisation for Scientific Research (NWO) for financial support in the form of a Solar Fuels Graduate Program. We thank the Netherlands Center for Multiscale Catalytic Energy conversion (MCEC), an NWO Gravitation program funded by the Ministry of Education, Culture and Science of the government of The Netherlands for the financial support with the AFM measurements. The authors thank Coen Mulder (Utrecht University, UU) and Christa van Oversteeg (UU) for the ICP-AES measurements, whereas Oscar Kerkenaar (UU), Pascal Wijten (UU), and Herrick Schaink (UU) are acknowledged for the technical support related to the GC measurements. K.C. acknowledges a research grant (9455) from VILLUM FONDEN. J.G. was supported by the U.S. Department of Energy, Chemical Sciences, Geosciences, and Biosciences (CSGB) Division of the Office of Basic Energy Sciences, via Grant DE-AC02-76SF00515 to the SUNCAT Center for Interface Science and Catalysis.

Conflict of interest

The authors declare no conflict of interest.

Keywords: electrocatalysis · electrodes · electrolytes · solar fuels · water splitting

[1] F. Safizadeh, E. Ghali, G. Houlachi, *Int. J. Hydrogen Energy* **2015**, *40*, 256–274.
[2] C. C. L. McCrory, S. Jung, I. M. Ferrer, S. M. Chatman, J. C. Peters, T. F. Jaramillo, *J. Am. Chem. Soc.* **2015**, *137*, 4347–4357.
[3] P. Gao, S. Li, X. Bu, S. Dang, Z. Liu, H. Wang, L. Zhong, Q. Minghuang, C. Yang, J. Cai, W. Wei, Y. Sun, *Nat. Chem.* **2017**, *9*, 1019–1024.
[4] M. G. Walter, E. L. Warren, J. R. McKone, S. W. Boettcher, Q. Mi, E. A. Santori, N. S. Lewis, *Chem. Rev.* **2010**, *110*, 6446–6473.
[5] F. Fresno, R. Portela, S. Suárez, J. M. Coronado, *J. Mater. Chem. A* **2014**, *2*, 2863–2888.
[6] A. R. Zeradjanin, J. Grote, G. Polymeros, K. J. J. Mayrhofer, *Electroanalysis* **2016**, *28*, 2256–2269.
[7] M. P. M. Kaninski, D. P. Saponjic, V. M. Nikolic, D. L. Zugic, G. S. Tasic, *Int. J. Hydrogen Energy* **2011**, *36*, 8864–8868.
[8] S. Zhao, J. Huang, Y. Liu, J. Shen, H. Wang, X. Yang, Y. Zhu, C. Li, *J. Mater. Chem. A* **2017**, *5*, 4207–4214.
[9] A. Kawashima, T. Sakaki, H. Habazaki, K. Hashimoto, *Mater. Sci. Eng.* **1999**, *267*, 246–253.
[10] C. González-Buch, I. Herraiz-Cardona, E. Ortega, J. García-Antón, V. Pérez-Herranz, *J. Appl. Electrochem.* **2016**, *46*, 791–803.
[11] A. Bigos, E. Beltowska-Lehman, M. Kot, *Surf. Coat. Technol.* **2017**, *317*, 103–109.
[12] R. Abdel-Karim, J. Halim, S. El-Raghy, M. Nabil, A. Waheed, *J. Alloys Compd.* **2012**, *530*, 85–90.
[13] N. V. Krstajic, V. D. Jovic, L. Gajic-Krstajic, B. M. Jovic, A. L. Antozzi, G. N. Martelli, *Int. J. Hydrogen Energy* **2008**, *33*, 3676–3687.
[14] G. S. Tasic, S. P. Maslovara, D. L. Zugic, A. D. Maksic, M. P. M. Kaninski, *Int. J. Hydrogen Energy* **2011**, *36*, 11588–11595.
[15] L. Zhang, K. Xiong, Y. Nie, X. Wang, J. Liao, Z. Wei, *J. Power Sources* **2015**, *297*, 413–418.
[16] S. J. Gutić, A. Z. Jovanovic, A. S. Dobrota, D. Metarapi, L. D. Rafailovic, I. A. Pasti, S. V. Mentus, *Int. J. Hydrogen Energy* **2017**, *43*, 16846–16858.
[17] J. R. McKone, B. F. Sadtler, C. A. Werlang, N. S. Lewis, H. B. Gray, *ACS Catal.* **2013**, *3*, 166–169.
[18] J. H. J. Wijten, R. P. H. Jong, G. Mul, B. M. Weckhuysen, *ChemSusChem* **2018**, *11*, 1374–1381.
[19] J. Halim, R. Abdel-Karim, S. El-Raghy, M. Nabil, A. Waheed, *J. Nanomater.* **2012**, 845673.
[20] M. Schalenbach, F. D. Speck, M. Ledendecker, O. Kasian, D. Goehl, A. M. Mingers, B. Breitbach, H. Springer, S. Cherevko, K. J. J. Mayrhofer, *Electrochim. Acta* **2018**, *259*, 1154–1161.
[21] Y. Wang, C. Woodward, S. H. Zhou, Z. K. Liu, L. Q. Chen, *Scr. Mater.* **2005**, *52*, 17–20.
[22] T. F. Jaramillo, K. P. Jørgensen, J. Bonde, J. H. Nielsen, S. Horch, I. Chorkendorff, *Science* **2007**, *317*, 100–103.
[23] Y. Yu, J. Zhang, W. Xiao, J. Wang, L. Wang, *Phys. Status Solidi B* **2017**, *254*, 1600810.
[24] Y. Yu, Q. Hu, W. Xiao, J. Wang, L. Wang, *Intermetallics* **2018**, *94*, 99–105.
[25] J. Greeley, J. K. Nørskov, L. A. Kibler, A. M. El-aziz, D. M. Kolb, *ChemPhysChem* **2006**, *7*, 1032–1035.
[26] J. K. Nørskov, T. Bligaard, A. Logadottir, J. R. Kitchin, J. G. Chen, S. Pandelov, U. Stimming, *J. Electrochem. Soc.* **2005**, *152*, J23–J26.
[27] B. Hinnemann, P. G. Moses, J. Bonde, K. P. Jørgensen, J. H. Nielsen, S. Horch, I. Chorkendorff, J. K. Nørskov, *J. Am. Chem. Soc.* **2005**, *127*, 5308–5309.
[28] J. Kibsgaard, C. Tsai, K. Chan, J. D. Benck, J. K. Nørskov, F. Abild-Pedersen, T. F. Jaramillo, *Energy Environ. Sci.* **2015**, *8*, 3022–3029.
[29] J. Greeley, T. F. Jaramillo, J. Bonde, I. Chorkendorff, J. K. Nørskov, *Mater. Sustainable Energy* **2010**, 280–284.
[30] K. Murase, M. Ogawa, T. Hirato, Y. Awakura, *J. Electrochem. Soc.* **2004**, *151*, C798–C805.
[31] L. S. Sanches, S. H. Domingues, C. E. B. Marino, L. H. Mascaro, *Electrochem. Commun.* **2004**, *6*, 543–548.
[32] E. J. Podlaha, D. Landolt, *J. Electrochem. Soc.* **1996**, *143*, 885–892.
[33] S. Djokic, *Electrodeposition and Surface Finishing*, Springer, New York, **2014**.
[34] http://Materialsproject.org **2018**, Ni, Mo, K, Na.
[35] T. J. P. Hersbach, V. A. Mints, F. Calle-Vallejo, A. I. Yanson, M. T. M. Koper, *Faraday Discuss.* **2016**, *193*, 207–222.
[36] T. J. P. Hersbach, A. I. Yanson, M. T. M. Koper, *Nat. Commun.* **2016**, *7*, 12653.
[37] P. M. Csernica, J. R. McKone, C. R. Mulzer, W. R. Dichtel, H. D. Abruna, J. DiSalvo, *ACS Catal.* **2017**, *7*, 3375–3383.
[38] M. Janssen, E. Griffioen, P. M. Biesheuvel, R. Van Roij, B. Erné, *Phys. Rev. Lett.* **2017**, *119*, 166002.
[39] S. Trasatti, O. A. Petrii, *J. Electroanal. Chem.* **1992**, *327*, 353–376.
[40] J. A. Olivares, R. S. Houk, *Anal. Chem.* **1986**, *58*, 20–25.
[41] G. Kresse, J. Hafner, *Phys. Rev. B* **1993**, *47*, 558–561.
[42] G. Kresse, J. Furthmüller, *Comput. Mater. Sci.* **1996**, *6*, 15–50.
[43] G. Kresse, J. Furthmüller, *Phys. Rev. B* **1996**, *54*, 11169–11186.
[44] G. Kresse, J. Hafner, *J. Phys. Condens. Matter* **1994**, *6*, 8245–8257.
[45] G. Kresse, D. Joubert, *Phys. Rev. B* **1999**, *59*, 1758–1775.
[46] B. Hammer, L. B. Hansen, J. K. No, *Phys. Rev. B* **1999**, *59*, 7413–7421.
[47] H. J. Monkhorst, J. D. Pack, *Phys. Rev. B* **1976**, *13*, 5188–5192.
[48] Y. Hirotsu, M. Uehara, M. Ueno, *J. Appl. Phys.* **1986**, *59*, 3081–3086.
[49] H. Ichinose, Y. Ishida, *Trans. Jpn. Inst. Met.* **1983**, *24*, 405–412.
[50] J. K. Nørskov, J. Rossmeisl, A. Logadottir, L. Lindqvist, J. R. Kitchin, T. Bligaard, H. Jonsson, *J. Phys. Chem. B* **2004**, *108*, 17886–17892.
[51] R. Dochertyt, G. Clydesdale, K. J. Roberts, P. Bennema, *J. Phys. D* **1991**, *24*, 89–99.
[52] E. L. Clark, J. Resasco, A. Landers, J. Lin, L. T. Chung, A. Walton, C. Hahn, T. F. Jaramillo, A. T. Bell, *ACS Catal.* **2018**, *8*, 6560–6570.
[53] Y. Yi, G. Weinberg, M. Prenzel, M. Greiner, S. Heumann, S. Becker, R. Schlögl, *Catal. Today* **2017**, *295*, 32–40.
[54] D. Nečas, P. Klapetek, *Open Phys.* **2012**, *10*, 181–188.

Manuscript received: March 3, 2019
Revised manuscript received: May 16, 2019
Accepted manuscript online: May 16, 2019
Version of record online: June 26, 2019

